J. Fluid Mech. (2012), *vol.* 711, *pp.* 192–211.
doi:10.1017/jfm.2012.387

Simulation and modelling of slip flow over surfaces grafted with polymer brushes and glycocalyx fibres

Mingge Deng[1], Xuejin Li[1], Haojun Liang[2], Bruce Caswell[3] and George Em Karniadakis[1]†

[1] Division of Applied Mathematics, Brown University, Providence, RI 02912, USA

[2] CAS Key Laboratory of Soft Matter Chemistry, Department of Polymer Science and Engineering, and Hefei National Laboratory for Physical Sciences at Microscale, University of Science and Technology of China, Hefei, Anhui 230026, PR China

[3] School of Engineering, Brown University, Providence, RI 02912, USA

(Received 6 February 2012; revised 20 June 2012; accepted 27 July 2012; first published online 3 September 2012)

Fabrication of functionalized surfaces using polymer brushes is a relatively simple process and parallels the presence of glycocalyx filaments coating the luminal surface of our vasculature. In this paper, we perform atomistic-like simulations based on dissipative particle dynamics (DPD) to study both polymer brushes and glycocalyx filaments subject to shear flow, and we apply mean-field theory to extract useful scaling arguments on their response. For polymer brushes, a weak shear flow has no effect on the brush density profile or its height, while the slip length is independent of the shear rate and is of the order of the brush mesh size as a result of screening by hydrodynamic interactions. However, for strong shear flow, the polymer brush is penetrated deeper and is deformed, with a corresponding decrease of the brush height and an increase of the slip length. The transition from the weak to the strong shear regime can be described by a simple 'blob' argument, leading to the scaling $\dot{\gamma}_0 \propto \sigma^{3/2}$, where $\dot{\gamma}_0$ is the critical transition shear rate and σ is the grafting density. Furthermore, in the strong shear regime, we observe a cyclic dynamic motion of individual polymers, causing a reversal in the direction of surface flow. To study the glycocalyx layer, we first assume a homogeneous flow that ignores the discrete effects of blood cells, and we simulate microchannel flows at different flow rates. Surprisingly, we find that, at low Reynolds number, the slip length decreases with the mean flow velocity, unlike the behaviour of polymer brushes, for which the slip length remains constant under similar conditions. (The slip length and brush height are measured with respect to polymer mesh size and polymer contour length, respectively.) We also performed additional DPD simulations of blood flow in a tube with walls having a glycocalyx layer and with the deformable red blood cells modelled accurately at the spectrin level. In this case, a plasma cell-free layer is formed, with thickness more than three times the glycocalyx layer. We then find our scaling arguments based on the homogeneous flow assumption to be valid for this physiologically correct case as well. Taken together, our findings point to the opposing roles of conformational entropy and bending rigidity – dominant effects for the brush and glycocalyx, respectively – which,

† Email address for correspondence: gk@dam.brown.edu

in turn, lead to different flow characteristics, despite the apparent similarity of the two systems.

Key words: biological fluid dynamics, low-Reynolds-number flows, non-Newtonian flows

1. Introduction

An effective way to design functionalized surfaces is to graft polymers onto the surface. Such tethered polymer chains or brushes have attracted a lot of attention in recent years for both engineering as well as biomedical applications, such as in stabilizing colloids (see Inn & Wang 1996), reducing friction between surfaces (see Klein *et al.* 1994) and designing novel microfluidic devices (see Adiga & Brenner 2005). Of particular interest on the biological side is the function of the glycocalyx layer coating the vessels in our vasculature (see Pries, Secomb & Gaehtgens 2000; Weinbaum, Tarbell & Damiano 2007).

The functioning of polymer brushes can be understood with the principles of excluded volume and conformational entropy. For dense polymer chains with one end attached to an impenetrable substrate and the other end left free, the excluded volume in the system will force the polymers to stretch away from the substrate (see Milner 1991*b*; Netz & Schick 1998; Deng *et al.* 2010). A relatively large number of *experimental* investigations (see Klein, Perahia & Warburg 1991; Klein *et al.* 1994; Baker *et al.* 2000; Ivkov *et al.* 2001; Anastassopoulos *et al.* 2006), *analytical* studies (see e.g. Rabin & Alexander 1990; Milner 1991*a*; Barrat 1992; Kumaran 1993; Sevick & Williams 1994; Aubouy, Harden & Cates 1996; Harden & Cates 1996) as well as *computational* simulations (see Lai & Binder 1993; Peters & Tildesley 1995; Miao, Guo & Zuckermann 1996; Grest 1996, 1999; Doyle, Shaqfeh & Gast 1997; Irfachsyad, Tildesley & Malfreyt 2002; Wijmans & Smit 2002; Kreer, Binder & Muser 2003; Huang, Wang & Laradji 2006; Pastorino *et al.* 2006; Müller & Pastorino 2008) have addressed the dynamics of polymer brushes exposed to fluid shear flow. However, it is still not well understood whether the polymer brushes show conformational changes, that is, swelling or collapse of the brush height at a certain value of shear rate. For example, Klein *et al.* (1991) reported a swelling of brush height of $\sim$25 % under strong shear flow in experiments, which has also been addressed by Barrat (1992) and Harden & Cates (1996) in theoretical studies. However, Baker *et al.* (2000) and Ivkov *et al.* (2001) observed in their experiments (using neutron and X-ray reflectivity techniques) that the polymer brush density profile and brush height remain unchanged when exposed to strong shear flow. In the computer simulations of Peters & Tildesley (1995), Miao *et al.* (1996) and Grest (1999), it was revealed that polymer chains were stretched and tilted towards the flow direction but the local density and the brush height did not change. These simulation studies are extensions of the theory by Rabin & Alexander (1990), who were the first to develop scaling approximations to quantify the amount of stretching that polymer brushes can withstand. In most of the theoretical and computer simulation studies published, tangential forces are employed to represent the shear flow, hence ignoring the hydrodynamic interactions in the system. Similarly, they may overestimate the penetration depth of shear flow inside the polymer brush when it is modelled as a porous medium based on Brinkman's equation (see Brinkman 1947). As shown by Milner (1991*a*), the relative penetration depth of a steady shear

flow is very small for brushes composed of long chains, and as a result only part of the polymer chain – instead of the entire chain – is directly affected by the shear flow.

On the biological side, the analogue of the polymer brush is the endothelial glycocalyx layer (EGL), which in reality is a macromolecular carbohydrate extracellular matrix, consisting of proteoglycans and glycoproteins that coat the luminal surface of the endothelial cells that line our vasculature. It is now well recognized that the EGL is critically important in many biological functions, and it can be viewed as a modulator for permeability in the trans-capillary exchange of water, as a mechanotransducer of fluid shear stress to the endothelial cytoskeleton, and as a regulator of blood-cell interactions (see Weinbaum *et al.* 2007). The EGL has also been considered as a potential diagnostic and therapeutic target in cardiovascular diseases, (see e.g. Broekhuizen 2009). Recently, several experimental studies have been reported on the EGL (see Squire *et al.* 2001; Gao & Lipowsky 2009); however, owing to its complexity, little has been done on its mathematical modelling. Damiano *et al.* (1996) and Damiano (1998) proposed a mixture theory model treating the EGL as a linearly elastic solid phase. Also, Secomb and coworkers used a Brinkman-type equation to represent the flow of the plasma within the EGL as a porous medium (see Secomb, Hsu & Pries 1998, 2001).

From the atomistic point of view, the glycocalyx layer should be modelled as a branched comb-like polymer brush, with fairly rigid core proteins (i.e. proteoglycans) bonded to the endothelial membrane, while the rest of the layer, consisting of much more flexible polymers, is directly connected to the core proteins. However, such atomistic level of detail is computationally prohibitive in the exploration of the *mesoscale properties* of the EGL. From the coarse-graining point of view, a branched comb-like polymer brush can be envisioned as a single semi-flexible chain consisting of impermeable blobs with size D_0; here, D_0 is the average size of side chains (see Birshtein *et al.* 1987; Zhulina & Vilgis 1995). Squire *et al.* (2001) proposed a model for the structural organization of the EGL, whereby the glycocalyx layer consists of uniform bonded elastic cylindrical beams with diameter $D_0 = 12$ nm, and with 20 nm taken as the distance between these beams. Based on this model, Weinbaum and coworkers developed a theoretical model to explore the deformability of the matrix due to interactions with the blood cells and in response to fluid shearing forces (see Guo, Weinstein & Weinbaum 2000; Weinbaum *et al.* 2003; Han *et al.* 2006). This work was the first to consider the flexural rigidity EI of the core proteins that represents resistance to the randomizing forces of Brownian motion and deformation by the fluid shear stress. The assumption behind these simplifications is that the biophysical and mechanical properties yielded by the models do not depend on the layer's detailed molecular topology. Thus, the model captures the average behaviour with assigned viscoelastic and transport properties. In our particle-based simulation, we coarse-grained the glycocalyx layer as a uniform semi-flexible brush, and then related our model to the beam model by its flexural rigidity and bending energy $EI = k_E b_0$. The tethered beads of glycocalyx filaments are fixed, which constraints them to bend instead of tilt when subject to a shear stress.

Both experimental and theoretical results have revealed that the EGL significantly influences the flow properties in small blood capillaries. However, up to now, the physical insight gained from this important but relatively unexplored bio-flow is still far from complete, and many open questions remain. The objective of the current work is to address fundamental questions on the behaviour of polymer brushes and glycocalyx fibres by performing direct numerical simulations of shear-driven and pressure-driven flows, and using mean-field theory (see Kim *et al.* 2009) to interpret

the simulation results. From the predictive modelling perspective, an accurate boundary condition for a polymer brush or glycocalyx attached to the surface is a crucial ingredient for efficient large-scale continuum fluid mechanical modelling of systems with such functionalized surfaces. We employ the dissipative particle dynamics (DPD) method, which can seamlessly model soft matter and fluid flow and explicitly includes hydrodynamic interactions. In addition, we use mean-field theory, which allows us to identify the most important parameters describing the models of the complex flows that we consider and to deduce appropriate scaling laws.

The paper is organized as follows. In § 2 we present the two different bead-and-spring models that we use to represent the brush and glycocalyx, and include some important simulation details along with a brief overview of DPD. In § 3 we present the simulation results and scaling arguments, first for polymer brushes and subsequently for the glycocalyx layer; in the latter case we also include high-resolution simulations of blood flow in a tube. We summarize our findings in § 4, and present the differences and similarities between the two flow systems.

2. Models and simulation details

We study the properties of polymer brushes and glycocalyx fibres subject to shear flow by employing DPD simulations. DPD is a mesoscale method for studying coarse-grained models of soft matter and complex fluid systems over relatively long length and time scales (see Hoogerbrugge & Koelman 1992; Groot & Warren 1997). In DPD, the particles interact via pairwise additive forces, consisting (in the basic form) of three components: (i) a conservative force $\boldsymbol{F}^C$; (ii) a dissipative force, $\boldsymbol{F}^D$; and (iii) a random force, $\boldsymbol{F}^R$. Hence, the total force on particle i is given by

$$\boldsymbol{F}_i = \sum_{i \neq j} \boldsymbol{F}_{ij}^C + \boldsymbol{F}_{ij}^D + \boldsymbol{F}_{ij}^R, \tag{2.1}$$

where the sum acts over all particles within a cutoff radius r_c. Specifically, in our simulations we have

$$\boldsymbol{F}_i = \sum_{i \neq j} a_{ij}\omega(r_{ij})\hat{\boldsymbol{r}}_{ij} - \gamma_* \omega^2(r_{ij})(\hat{\boldsymbol{r}}_{ij} \cdot \hat{\boldsymbol{v}}_{ij})\hat{\boldsymbol{r}}_{ij} + \sigma_* \omega(r_{ij})\zeta_{ij}\Delta t^{-1/2}\hat{\boldsymbol{r}}_{ij}, \tag{2.2}$$

where a_{ij} is a maximum repulsion between particles i and j. In the polymer brush simulations, we set $a_{pp} = a_{ss} = 25.0$; here, p and s denote polymer and solvent particles, respectively. We also choose $a_{ps} = 27.2$ to represent a *theta solvent* condition and $a_{ps} = 20.0$ to represent a *good solvent* condition (see Nardai & Zifferer 2009). Also, r_{ij} is the distance with the corresponding unit vector $\hat{\boldsymbol{r}}_{ij}$, $\hat{\boldsymbol{v}}_{ij}$ is the difference between the two velocities, ζ_{ij} is a random number with zero mean and unit variance, and γ_* and σ_* are parameters coupled by $\sigma_*^2 = 2\gamma_* k_B T$ (see Espanol & Warren 1995; Lei, Caswell & Karniadakis 2010). Typically, the weighting functions $\omega(r_{ij})$ are given by

$$\omega\left(r_{ij}\right) = \begin{cases} 1 - \dfrac{r_{ij}}{r_c}, & r_{ij} < r_c, \\ 0, & r_{ij} \geqslant r_c. \end{cases} \tag{2.3}$$

The above system of equations models the solvent but using the DPD approach we can also model the polymer brush or the glycocalyx as a bead–spring chain with $N = 36$ segments for the polymer brush and $N = 21$ segments for the glycocalyx filament. This choice is based on the physics of the corresponding chains, and in

particular the fact that the dynamics of polymer brushes is entropy-dominated and hence its corresponding radius of gyration is greater than its segment length. The neighbouring particles are joined by harmonic springs with constant $k_b = 100.0$ and equilibrium bond length $b_0 = 0.86$, selected so that the thermal fluctuations do not affect the bond length, i.e.

$$F_{ij}^S = k_b(1 - r_{ij}/b_0)\hat{\boldsymbol{r}}_{ij.} \tag{2.4}$$

We note that the tethered bead of the brush polymer is free to rotate, whereas that of the glycocalyx is fixed. Grafting in both cases is uniform, with chains perpendicular to the wall. All simulations are three-dimensional and hence the chains are allowed to move in all three directions. In the following we provide simulation details separately for the polymer brush and the glycocalyx.

2.1. *Polymer brushes*

We consider shear flow over a surface grafted with polymer brushes in a *three-dimensional* channel (of width D), where one of the channel walls is moving in the flow direction (x) with constant velocity to impose an apparent shear rate. An adaptive no-slip boundary condition is employed at $z = 0$ and $z = D$ to eliminate any spurious density and thermal fluctuations near the wall (see Fedosov & Karniadakis 2009). The polymer brush is constructed by tethering one end of the chains at the surface at $z = 0$. Periodic boundary conditions are applied along the y (spanwise) and x (streamwise) directions. The average particle number density of the DPD solvent is $\rho = 3.0r_c^{-3}$ and the temperature is set with $k_BT = 1.0$. The simulations are performed using a modified version of the DPD code based on the open-source code LAMMPS (see Plimpton 2011). Time intergation of the equation of motion is obtained by a modified velocity–Verlert algorithm, first proposed by Groot & Warren (1997), with time step $\Delta t = 0.005$ (in DPD time units).

2.2. *Glycocalyx*

Here we study the response of the glycocalyx to a pressure-driven microchannel flow. We choose a slightly different weighting function in order to increase the value of the solvent viscosity, i.e. $\omega(r_{ij}) = (1 - r_{ij}/r_c)^{1/4}$ when $r_{ij} < r_c$, and $\omega(r_{ij}) = 0$ when $r_{ij} \geqslant r_c$. To the DPD model of the glycocalyx filaments, described above, as bead–spring chains, we add bending energy to give a semi-flexible chain. For each segment the bending energy is

$$E_{bend} = \tfrac{1}{2}k_E\,(\theta - \theta_0)^2, \tag{2.5}$$

where $\theta_0 = \pi$ is the equilibrium angle between three neighbouring particles, and the harmonic bending constant k_E is related to the flexural rigidity of the glycocalyx filament according to the Euler–Bernoulli beam theory, i.e. $EI = k_Eb_0$. In the current work, we study pressure-driven flow over the glycocalyx layer in a slit channel with length L_c and width D. We will present results first for a channel with width $D = 3$ μm and $D = 5$ μm as well as for a tube with diameter $D = 10$ μm. An adaptive no-slip boundary condition is also employed for this case at $z = -D/2$ and $z = D/2$, similarly to the polymer brush simulations. The glycocalyx layer is constructed by tethering one end of the glycocalyx chains at the wall surface. The flow of the solvent in the slit is sustained by applying a constant body force along the flow (x) direction on each flow particle, while periodic boundary conditions are applied in the cross-flow (y) direction. The average particle number density of the DPD solvent is $\rho = 3.0r_c^{-3}$ and

the temperature is set with $k_BT = 0.1$, while time integration of the motion equation is obtained again by employing the modified velocity–Verlet algorithm with time step $\Delta t = 0.001$ (in DPD time units).

3. Simulation results

In this section we present simulation results and scaling laws for the polymer brush and glycocalyx fibres in shear-driven and pressure-driven flows, respectively. In addition, we present simulation results for a model blood suspension flowing in a tube coated with a glycocalyx layer, hence resembling a small arteriole. In both shear flow and pressure-driven flow cases, the flow particles (represented by DPD) are assumed to be at rest initially. For shear flow we suddenly move the upper wall constructed by frozen DPD particles with a constant velocity. For the pressure-driven case, the flow is sustained by a constant body force applied to every flow particle. Steady states were achieved relatively quickly, but we ran for one million time steps to ensure that the velocity field remains stationary in time. All physical quantities of the system were measured after reaching stationarity by a binning procedure in space and applying time averaging.

3.1. *Polymer brushes*

We first present validation results in equilibrium followed by simulations under shear flow and the development of scaling laws. We also include a brief section on how to map the DPD simulation units into physical units.

3.1.1. *Validation*

We first verify the accuracy of the DPD fluid–brush model by performing simulations in the absence of flow in both *good* and *theta* solvents. According to accepted published results, polymer brush density profiles change from parabolic functions (of distance to the wall) to step-like functions with increasing grafting density from moderate to very large values. The equilibrium properties of polymer brushes are determined by the excluded-volume interaction and the conformational entropy of the polymer chains, which yield a scaling law for the brush height (see Alexander 1977; de Gennes 1980; Milner, Witten & Cates 1988; Zhulina, Borisov & Pryamitsyn 1990; Kent *et al.* 1995), as follows:

$$h \sim L\,(\sigma b^2)^{(1/\nu-1)/2} \tag{3.1}$$

where σ is the grafting density, ν is the Flory exponent, and $L = Nb$ is the contour length of polymer, with N the number of beads. The average brush height h is calculated from the first moment of the density profiles of polymer monomers, i.e.

$$h = 2\frac{\int z\rho(z)\,\mathrm{d}z}{\int \rho(z)\,\mathrm{d}z}. \tag{3.2}$$

The factor 2 is included in the equation for normalization, i.e. to recover the correct value in the case of uniform monomer density profile inside the brush. In figures 1 and 2 we show our simulation results for theta and good solvents, which are in agreement with the theoretical scaling results denoted by the dotted lines, corresponding to slopes of $1/2$ and $1/3$, respectively.

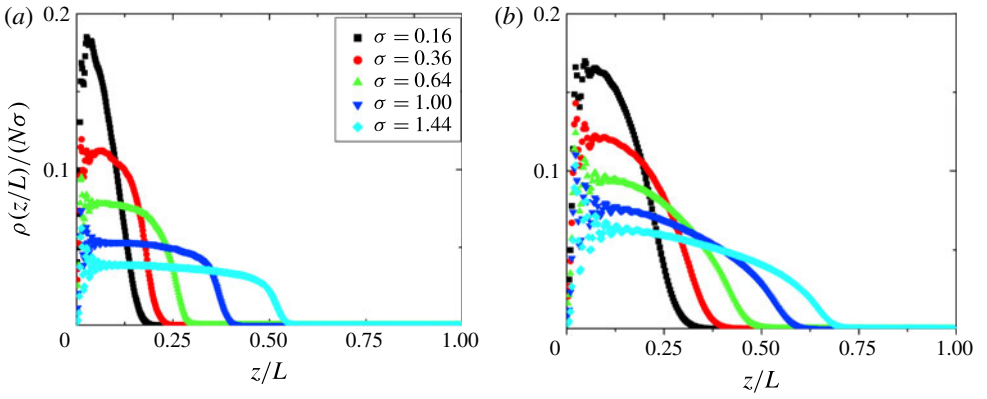

FIGURE 1. (Colour online) Normalized monomer density profile of a polymer brush in (*a*) theta solvent and (*b*) good solvent for different grafting densities σ. (The wiggles around $z = 0$ are due to the binning procedure.)

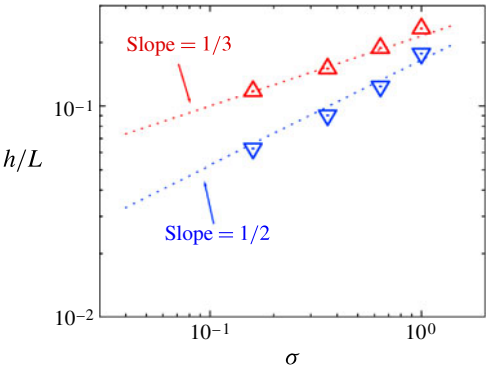

FIGURE 2. (Colour online) Polymer brush height as a function of grafting density for a theta solvent (inverted triangles (blue online)) and for a good solvent (triangles (red online)). The dotted lines represent the known scaling relations.

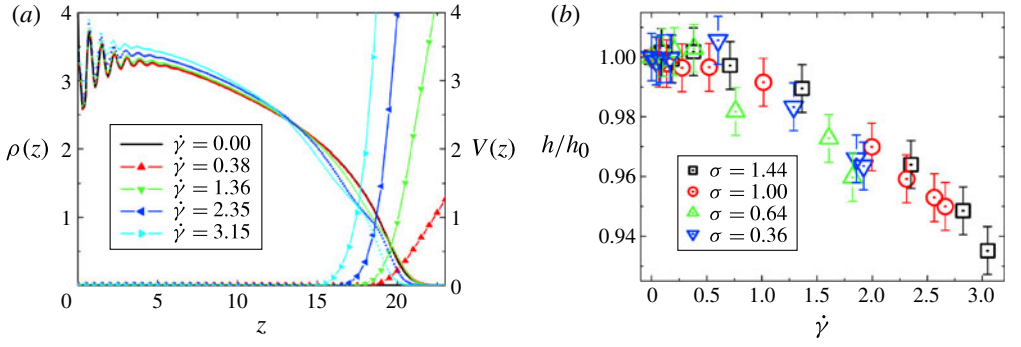

FIGURE 3. (Colour online) (*a*) Monomer density profiles and flow velocity profiles normal to the flow direction for grafting density $\sigma = 1.44$ under different shear rates. (The wiggles are due to the binning procedure.) (*b*) Relative brush height as a function of shear rate for different grafting densities. The denominator h_0 represents the original brush height without shear flow.

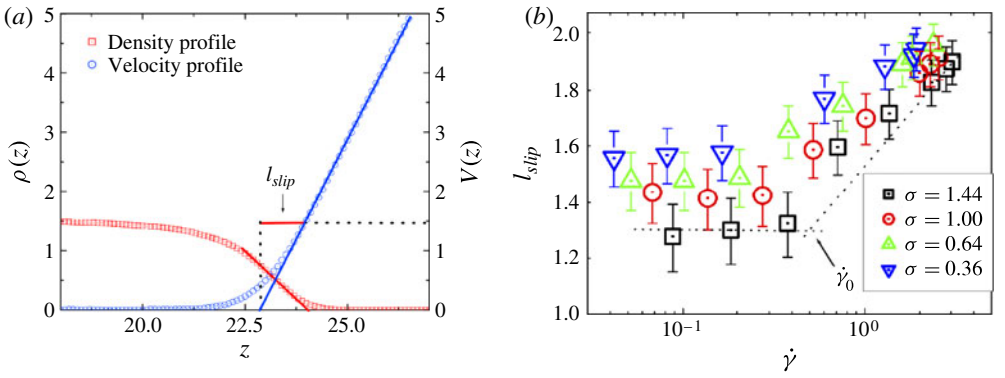

FIGURE 4. (Colour online) (*a*) Density and velocity profiles magnified around the zero values and sketch of the definition of slip length. (*b*) Slip length as a function of shear rate for different grafting densities; $\dot{\gamma}_0$ is the critical shear rate when flow starts to penetrate deeper into the brush.

3.1.2. *Scaling laws*

The influence of the shear flow on the polymer brush density profiles in the direction perpendicular to the grafting plane is shown in figure 3(*a*). We see that, as expected, for low shear rates the density profiles do not differ from the equilibrium profile, whereas for larger shear rates the brush physically thins in the free-end region. Overall, the density profiles do not change substantially; however, the flow is affected greatly inside the brush, as is evident from the profiles shown in the same figure. In order to quantify more precisely the compression of the brush, we calculated the relative average brush height under shear flow for different grafting densities in figure 3(*b*). We see that, for shear rates lower than a critical value ($\dot{\gamma}_0 \approx 0.5$ in DPD units), there is no compression at all, while only a 5 % decrease is obtained by increasing the shear rate by 300 % beyond the critical value $\dot{\gamma}_0$. These simulation results are consistent with the simulations of Lai & Binder (1993) and Doyle *et al.* (1997) obtained using different methods. However, our results invalidate the theory by Barrat (1992), who argued that increasing the shear rate will lead to increases of the average brush height h.

An intriguing physical property of a polymer brush under shear flow is the hydrodynamic penetration depth l_{slip}, also called *slip length*, which is defined from extrapolation of the far-field linear region of the velocity profile to the z axis as shown in figure 4(*a*). The velocity penetrates only a small portion of the brush and decreases rapidly inside it. The same far-field velocity profile in figure 4(*a*) can be obtained by replacing the brush with a solid surface of thickness $(h - l_{slip})$. The slip length is of the order of the brush mesh size (average distance between two beads), ξ_0, i.e. $l_{slip} \sim \xi_0 \sim b/\sigma^{1/2}$ according to the 'blob theory' of Rabin & Alexander (1990). This value is smaller than the one suggested by Milner (1991*b*) for a 'parabolic' polymer brush ($l_{slip}/\xi_0 \sim (N\sigma b^2)^{1/2}$) due to the screening of hydrodynamic interactions. In figure 4(*b*) we plot the slip length versus the shear rate (in DPD units) for different values of the grafting density. We see that l_{slip} is independent of the shear rate below the critical value $\dot{\gamma}_0$ that we identified in figure 3(*b*) but grows linearly beyond that value.

Based on the above results, it is clear that there are two different regimes characterizing the polymer brush dynamics, namely the *weak* shear flow regime and

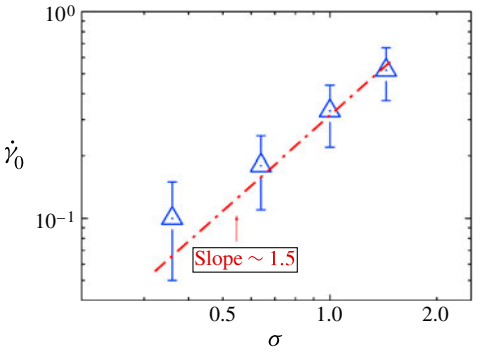

FIGURE 5. (Colour online) Critical shear rate $\dot{\gamma}_0$ as a function of grafting density. The dashed-dotted line represents the scaling law based on the 'blob argument'.

the *strong* shear flow regime. In the former, the conformation of the polymer brush is not disturbed (up to the critical shear rate value) while the slip length remains equal to the mesh size of the polymer brush. In the latter, the polymer brush is penetrated deeper by the solvent, its free end is slightly compressed, and the slip length increases with shear rate.

Next, we use a simple 'blob scaling' argument to gain some insight into the characteristics of the weak and strong shear flow regimes. Based on the studies of Alexander (1977) and of de Gennes (1980), a grafted polymer can be modelled as a string of blobs, but only a small part of the blobs – rather than the entire polymer chains – are directly affected by the shear due to the hydrodynamic screening. Hence, brush compression is expected when the flow is able to stretch chains inside the outer blob of brush beyond the Gaussian regime of elasticity. The Weissenberg number inside the outer blob is $W_i = \dot{\gamma}\tau$, where $\dot{\gamma}$ is the unscreening shear rate and τ is the characteristic relaxation time for the polymer chain affected by the shear flow with length l_{slip}. Using the Rouse model we have that $\tau \sim \eta_s l_{slip}^3/k_BT$, where η_s is the viscosity of the solvent. Under small shear rates, as mentioned above, $l_{slip} \sim \xi_0 \sim b/\sigma^{1/2}$, thus,

$$W_i \sim \dot{\gamma}\tau \sim \eta_s \dot{\gamma}\sigma^{-3/2}/k_BT \sim 1. \tag{3.3}$$

This leads to the following relation between the critical shear rate and the grafting density:

$$\dot{\gamma}_0 \sim \sigma^{3/2}. \tag{3.4}$$

Figure 5 shows the relationship between these two parameters. The critical shear rate data are directly determined through figure 4(*b*); our simulation results are consistent with the scaling argument. The small discrepancy at the smallest grafting density value is apparently due to the density profile departure from the parabolic shape assumed in the blob model analysis. The slip length is a function of shear rate $\dot{\gamma}$, of the grafting density σ and also of the solvent condition (Flory exponent ν), which can be written as

$$\frac{l_{slip}}{\sigma^{-1/2}} \sim 1 + f(\dot{\gamma} - \dot{\gamma}_0, \nu), \tag{3.5}$$

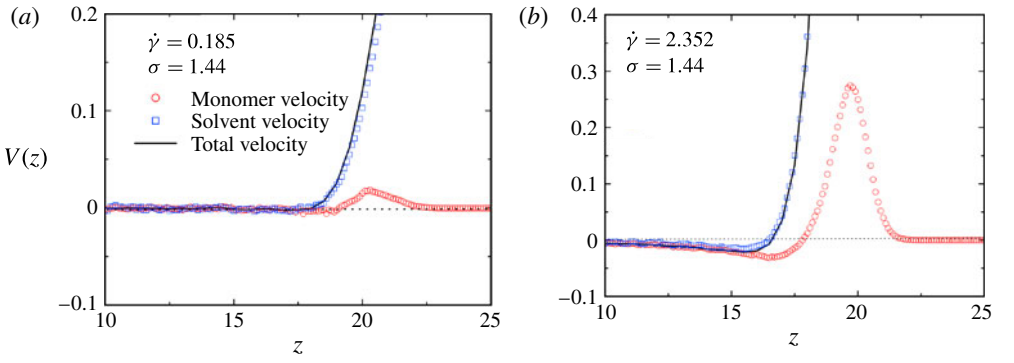

FIGURE 6. (Colour online) Velocity distributions near the solvent and polymer brush interface: (*a*) under weak shear flow; and (*b*) under strong shear flow.

where f is a step-like function of the form

$$f(\dot{\gamma} - \dot{\gamma}_0, \nu) = \begin{cases} 0, & \text{for } \dot{\gamma} < \dot{\gamma}_0, \\ (\dot{\gamma} - \dot{\gamma}_0)^{\alpha(\nu)}, & \text{for } \dot{\gamma} \geqslant \dot{\gamma}_0. \end{cases} \tag{3.6}$$

3.1.3. *Flow structure*

Next we investigate the flow structure inside the polymer brushes. It was found recently by Müller & Pastorino (2008) using molecular dynamics that untangled polymer chains in a dense brush exhibit cyclic and tumbling motion, which is similar to the behaviour of isolated tethered chains in shear flow. Their results show that the collective molecular motion leads to a reversal of the flow direction in the vicinity of the brush-grafted surface. This was also observed in our DPD simulations, as shown in figure 6. In the weak shear rate regime, there is no cyclic or tumbling motion of individual polymers near the surface and the velocity is positive there. However, in the strong shear rate regime, there is a considerable effect on the polymer brush with the cyclic and tumbling motion leading to a negative velocity near the surface and hence flow reversal.

3.1.4. *Physical units*

Next we map the DPD units to the physical units in order to be able to compare the magnitude of slip length and critical shear to experimental values. To this end, we need to consider as reference a specific experimental system, e.g. polystyrene brushes in good solvent (toluene) under conditions of strong shear flow (see Anastassopoulos *et al.* 2006). The superscript P denotes 'physical' while the superscript S denotes 'simulation' in the following scaling formulas. First, we define the length scale

$$r_c = \frac{(\sigma^P)^{-1/2}}{(\sigma^S)^{-1/2}} \text{ m}, \tag{3.7}$$

where 'm' stands for 'metre'. Then, the time units are scaled with the critical shear rate as (with 's' indicating 'second')

$$\tau = \frac{(\dot{\gamma}_0^P)^{-1}}{(\dot{\gamma}_0^S)^{-1}} \text{ s}, \tag{3.8}$$

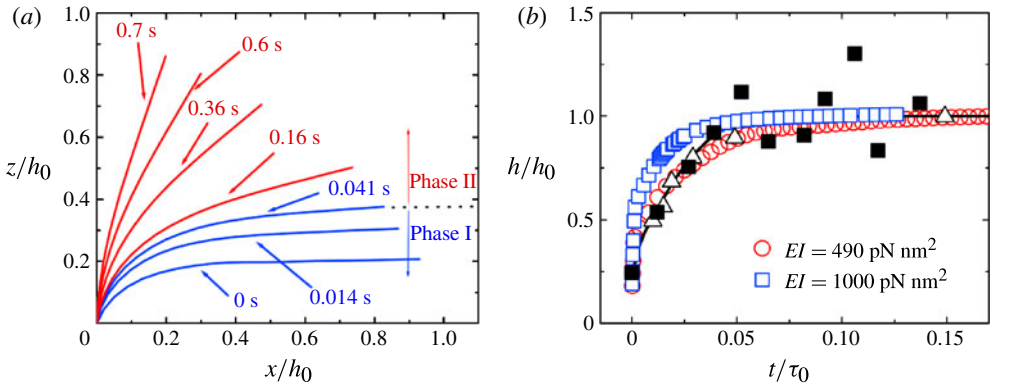

FIGURE 7. (Colour online) Large glycocalyx deformation. (*a*) Time-dependent change in the shape of a glycocalyx fibre with $EI = 490$ pN nm^2, mimicking the passing of a white blood cell. (*b*) Comparison of our simulation results with theoretical predictions in Han *et al.* (2006) (solid line) and in Damiano & Stace (2002) (open triangles), as well as with experimental results in Han *et al.* (2006) (solid squares). Here $\tau_0 = 14$ s is a dimensional scaling factor related to the flexural rigidity $EI = 490$ pN nm^2.

and the force units (where 'N' denotes 'newton') are scaled with the viscosity of toluene as

$$\mathrm{N}^S = \frac{\eta^P \dot{\gamma}_0^P \sigma^S}{\eta^S \dot{\gamma}_0^S \sigma^P}\,\mathrm{N}^P. \tag{3.9}$$

To give specific physical values, we will refer to the experimental set-up of Anastassopoulos *et al.* (2006) of a polymer brush with relatively high grafting density. We use $\sigma^S = 1.00$ for the grafting density in DPD units in our simulation, which corresponds to the physical value $\sigma^P = 0.1276$ nm^{-2} in the experimental system of Anastassopoulos *et al.* (2006). Then, the unit length scale is $r_c = 2.8$ nm according to (3.7), and the corresponding slip length is of the order of several nanometres. By matching the critical shear rate for the same grafting density, $\dot{\gamma}_0^P = 10^6$ s^{-1} and $\dot{\gamma}_0^S = 0.345\ \tau^{-1}$, we obtain the time scale $\tau = 3.45 \times 10^{-6}$ s according to (3.8). The force units are scaled with the viscosity of toluene ($\eta^P = 6.0 \times 10^{-4}$ Pa s) using (3.9), which is $\sim 1.31 \times 10^{-2}$ pN in our simulation.

3.2. *Glycocalyx*

The main difference between the polymer brushes that we have modelled above and the glycocalyx fibres we consider next is that the dynamics of the brush is dominated by its conformational entropy whereas the dynamics of the glycocalyx is dominated by its *bending energy*. Hence, we model the glycocalyx as a *semi-flexible* polymer as we discussed above in § 2.2.

3.2.1. *Validation*

First, we validate the DPD fluid–glycocalyx model under time-dependent conditions. An interesting feature of the glycocalyx layer is the elastic recoiling after *large deformation*, which, for example, may take place after the passage of a white blood cell through a small capillary. The time-dependent restoration of the glycocalyx layer has been studied both experimentally as well as theoretically using large-deformation analysis (see Han *et al.* 2006). There are two distinct phases of filament recoil as

shown in figure 7(*a*): an initial phase (phase I, lowermost three lines (blue online)) for large compressions, where the ends of the fibre overlap and are parallel to the capillary wall; and a second phase (phase II, uppermost four lines (red online)), where the slope at the fibre tip continues to increase as the fibre recoils back to its original shape. The second phase is a much slower recoiling process compared to the initial phase. We computed the glycocalyx layer height as a function of time and compared it with both theoretical and experimental results for the case with $EI = 490$ pN nm^2. Our simulation results are in good agreement with previous studies, as shown in figure 7(*b*), which provides a further validation of our coarse-grained glycocalyx fibre model.

3.2.2. *Mean-field theory*

The mean-field theory model of Kim *et al.* (2009) treats a single glycocalyx fibre in its most likely configuration, namely, the ground state, and subject to the hydrodynamic drag force of the solvent flow. The configuration of the glycocalyx fibre is described by a continuous space curve along the fibre using the arc variable s, defined as: $s = 0$ at the grafted end, and $s = l$ at the free end. We assume that the fibre lies in the x–z plane and we describe its shape by the angle $\theta(s)$. The potential of the mean force functional of the semi-flexible chain consists of the bending energy and the work done by the drag force (i.e. the term $\gamma u(z)$ in the equation below):

$$E[\theta, u] = \int_0^l \left[\frac{1}{2}k_b\dot{\theta}(s)^2 - [\gamma u(z(s)) - b_0^2 q]x(s)\right] \mathrm{d}s, \tag{3.10}$$

where $x(s) = \int_0^s \mathrm{d}s' \sin\theta(s')$ and $z(s) = \int_0^s \mathrm{d}s' \cos\theta(s')$ determine the chain shape, $q = \mathrm{d}p/\mathrm{d}x = (P_{out} - P_{in})/L$ describes the pressure drop along the flow direction, $\gamma = 3\pi\eta$ is the friction coefficient per unit length, and η is the dynamic viscosity of the fluid. Unlike the polymer brush modelling, here we have neglected the excluded-volume interactions between glycocalyx fibres. This is justified since the glycocalyx fibres are immersed in blood plasma, which contains the same main components as the glycocalyx layer, i.e. glycoproteins and other soluble proteins. Therefore, the interactions between the glycocalyx fibres are screened by blood plasma, similar to the case of a polymer having the same behaviour in a melt and a theta solvent.

Using the mean velocity field approximation and neglecting the fluctuations of the glycocalyx fibres, the most likely configuration is achieved by minimizing the functional $E[\theta, u]$. To this end, we differentiate with respect to $\theta(s)$, leading to

$$k_b\ddot{\theta}(s) = -\cos\theta(s)\int_s^l \mathrm{d}s' \,[\gamma u(s') - b_0^2 q]. \tag{3.11}$$

The solvent flow can be described by a two-layer model, with the equation governing the velocity of the fluid above the glycocalyx layer given by $\eta(\mathrm{d}^2u_1(z)/\mathrm{d}z^2) = q$ with $\mathrm{d}u_1(z)/\mathrm{d}z|_{z=D/2} = 0$; the latter reflects the symmetry condition of the geometry in this problem. However, within the EGL, we use a modified Brinkman equation in which the deformation of the glycocalyx fibre is included, i.e.

$$\eta\frac{\mathrm{d}^2u_2(z)}{\mathrm{d}z^2} = \gamma\sigma\frac{u_2(z)}{\cos\theta(z)} + q, \tag{3.12}$$

where σ is the EGL grafting density. We note that for $\theta = \pi/2$ the glycocalyx fibres are parallel to the wall, making them a part of the solid wall, and hence the singular

limit in the above equation. Equation (3.12) can be reparametrized as

$$\cos\theta(s)\frac{\mathrm{d}^2u_2(s)}{\mathrm{d}s^2}+\sin\theta(s)\frac{\mathrm{d}\theta}{\mathrm{d}s}=\frac{\gamma\sigma}{\eta}\cos^2\theta(s)u_2(s)+\frac{q}{\eta}\cos^3\theta(s), \tag{3.13}$$

with boundary condition $u_2(s)|_{s=0}=0$. Both velocity and shear stress should be continuous at the glycocalyx–free solvent interface, and hence

$$\begin{cases} u_1(z)|_{z=h}=u_2(z)|_{z=h}, \\ \eta\dfrac{\mathrm{d}u_1(z)}{\mathrm{d}z}\bigg|_{z=h}=\eta\dfrac{\mathrm{d}u_2(z)}{\mathrm{d}z}\bigg|_{z=h}+\gamma u_2(z), \end{cases} \tag{3.14}$$

where $h=\int_0^l \mathrm{d}s'\cos\theta(s')$ describes the height of glycocalyx fibres. We solved the system of equations (3.11), (3.13) and (3.14) using a second-order finite difference method to obtain the most likely conformation of the glycocalyx fibre and the corresponding velocity field.

3.2.3. *DPD simulations*

Next, we proceed with the DPD simulations, but we first need to scale the DPD units to physical units as follows: lengths are normalized with the glycocalyx layer height h^P, i.e. $r_c=(h^P/h^S)$ m, where (as before) the superscript P denotes 'physical', superscript S denotes 'simulation' and 'm' denotes 'metre'. It is natural to involve the flexural rigidity EI into the scaling as the key parameter. Matching the physical and simulation flexural rigidity EI^S N^S $r_c^2=EI^P$ N^P m^2 provides the force scaling

$$\mathrm{N}^S=\frac{EI^P}{EI^S}\,\frac{\mathrm{m}^2}{r_c^2}\,\mathrm{N}^P=\frac{EI^P}{EI^S}\left(\frac{h^S}{h^P}\right)^2\mathrm{N}^P. \tag{3.15}$$

Also, by matching the dynamic viscosities of the blood plasma and the simulation fluid, η^S (N^S/r_c^2) $\tau=\eta^P$ $(\mathrm{N}^P/\mathrm{m}^2)$ s, we obtain the time scaling

$$\tau=\frac{\eta^P}{\eta^S}\,\frac{\mathrm{N}^P}{\mathrm{N}^S}\,\frac{r_c^2}{\mathrm{m}^2}\,\mathrm{s}=\frac{\eta^P}{\eta^S}\,\frac{EI^S}{EI^P}\left(\frac{h^P}{h^S}\right)^4\mathrm{s}. \tag{3.16}$$

Based on the aforementioned observations, we introduce a dimensionless parameter

$$A=({h_0}^2/EI)(h_0-D/2)q/\sigma \tag{3.17}$$

that characterizes the relative deformation properties of the glycocalyx fibre subjected to a pressure-driven flow in a small channel. (Here h_0 is the length of the undisturbed EGL fibres.) This parameter also represents the relative drag force on the tip of the glycocalyx fibre compared to the recoiling force of the glycocalyx due to its original flexural rigidity EI when the deformation of the glycocalyx fibre is relatively small and $D\gg h_0$. Although this may look like an *ad hoc* choice, it is justified by our simulation results, as we found that all of the physical properties in the problem we consider can be represented as simple functions of A, as will be shown below.

First, we present velocity profiles of the pressure-driven flows over the EGL for different EI in figure 8(*a*); the effective width of the channel decreases as EI increases, and there is an exponential rather than linear velocity distribution near the glycocalyx and free flow interface, as shown in the inset of figure 8(*a*). These results show a significant effect of the glycocalyx layer on the flow inside the channel. From experimental observations we know that the resistance in microvessels is higher than expected based on the rheological behaviour of blood in glass tubes, and this

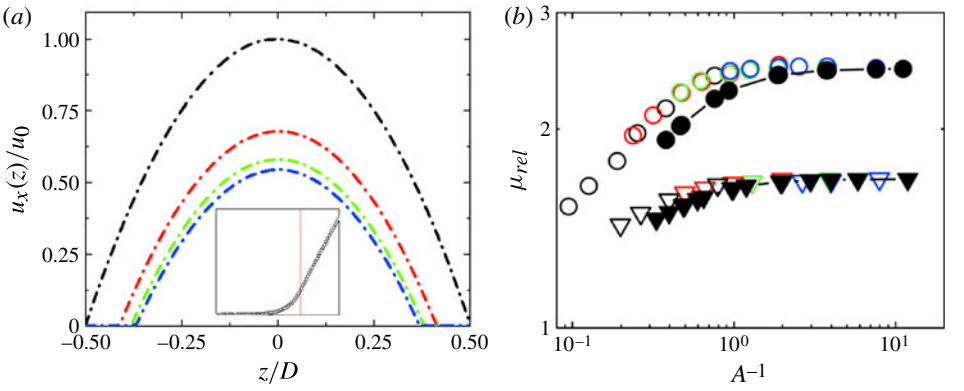

FIGURE 8. (Colour online) Flow in a microchannel endowed with a glycocalyx on both walls. (*a*) Normalized velocity profiles with different flexural rigidity EI; from the top downwards, the black line represents results without glycocalyx, while the red, green and blue lines represent results in the presence of glycocalyx for $EI = 100,\ 200,\ +\infty$ pN nm^2. The inset is a zoomed velocity profile near the glycocalyx–fluid boundary. (*b*) Relative apparent viscosity as a function of the dimensionless characteristic parameter A; the circles and inverted triangles represent the results of the 3 and 5 μm channels, respectively, while the open and solid symbols represent the results from DPD simulation and mean-field theory, respectively.

difference is attributed to the presence of the glycocalyx layer and the effects of irregular vessel shape (see Pries *et al.* 1994; Pries & Secomb 2005). Specifically, direct measurements of the resistance to blood flow through microvascular networks showed that the resistance was more than twice that of flow in glass tubes (see Pries *et al.* 1994). As shown in figure 8(*b*), the relative apparent viscosity, which is defined as $\mu_{rel} = \eta_{app}/\eta$ (with $\eta_{app} = qD^2/(12\bar{u})$, $\bar{u}$ is the mean velocity across the channel), agrees with experimental results and moreover it seems to be a unique function of the dimensionless parameter A, since all the data for different values of the parameters, such as EI, σ, q, etc., collapse onto a single curve.

It is also important to quantify the exact deformation of the glycocalyx in order to determine the surface boundary conditions. Hence, we investigated the dependence of the *small deformation* on the flexural rigidity as well as the shear stress in our DPD simulations. In particular, $h \sim h_0\langle\cos\theta\rangle$, and thus $\Delta h \sim h_0\langle 1-\cos\theta\rangle \sim h_0\langle\theta^2\rangle/2$. Based on this small-deformation approximation, the relative decrease of the glycocalyx height can be described by a simple scaling argument as follows:

$$\frac{\Delta h}{h_0} \sim \left(\frac{f{h_0}^2}{EI}\right)^2 \sim \left(\frac{{h_0}^2}{EI}\frac{(h_0 - D/2)q}{\sigma}\right)^2. \tag{3.18}$$

Here $\Delta h = h_0 - h$ describes the decrease in the height of the EGL fibres, and $\langle\theta\rangle$ is the average angle between the glycocalyx fibre and the main flow direction induced by the drag force f. As shown in figure 9(*b*), both our mean-field calculation and DPD simulation results are consistent with this simple scaling argument when the deformation is small. We also note that the case $EI = 0$ (corresponding to a model for a polymer brush) scales differently, i.e. the height is constant irrespective of the mean flow velocity for such low Reynolds numbers (less than 0.001). This result was also

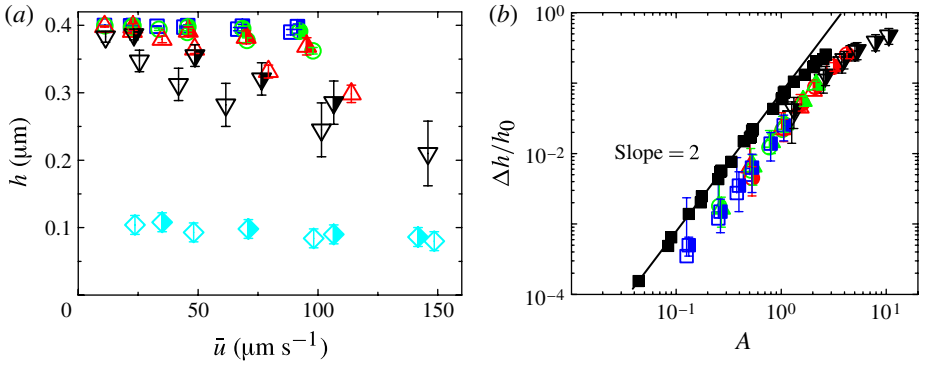

FIGURE 9. (Colour online) Flow over the glycocalyx. (*a*) EGL height as a function of the mean velocity across the channel. (*b*) Relative decrease of EGL height as a function of A. The solid line and black solid squares represent the scaling law and mean-field calculation results, respectively. The open symbols and half-open symbols represent DPD simulation results of 5 and 3 μm channels, respectively; the square, circle, upper-triangle, lower-triangle and diamond symbols represent EGL fibre with $EI = 1000, 490, 250, 100, 0$ pN nm^2, respectively.

obtained in the previous section for polymer brushes in the weak shear rate regime for a Couette-like flow system.

Next, we study the partial slip properties by computing the slip length at the glycocalyx layer surface, which is defined by the extrapolation of the far-field linear region of the velocity profile to the z axis. The velocity profile penetrates only a small portion (∼5–10 % of the glycocalyx layer height in our simulation) of the glycocalyx layer and decreases rapidly inside this layer. The same far-field velocity profile can be obtained by replacing the EGL with a surface of thickness $(h - l_{slip})$ and prescribing the slip boundary condition; hence it is important to know the exact slip boundary condition for continuum fluid calculations. Surprisingly, despite the complexity of the system, the dimensionless slip length (normalized by the average distance between glycocalyx fibres) is a simple linear function of the relative decrease of the glycocalyx height by the flow, when the deformation of the glycocalyx is small, which is related to the parameter A defined earlier, i.e.

$$\frac{l_{slip}}{\sigma^{-1/2}} \sim -\frac{\Delta h}{h_0} \sim -\left(\frac{{h_0}^2}{EI}\frac{(h_0 - D/2)q}{\sigma}\right)^2 \sim -A^2. \tag{3.19}$$

This scaling is also verified by our mean-field theory calculation, as shown in figure 10.

Using linear analysis, Kim *et al.* (2009) have shown that the semi-flexible polymer brush height follows a quadratic dependence on the ratio of shear rate and persistence length (see equation (14) of Kim *et al.* (2009)), which agrees with our simulation results. However, the slip length does not depend on shear rate or persistence length but does depend on the grafting density according to the analysis of Kim *et al.* (2009). Our simulation results suggest that the slip length is a function of both shear rate and persistence length, which is consistent with the experimental data and the Brownian dynamics simulation results of Kim *et al.* (2009) (see their figure 4). In particular, the slip length decreases with increasing shear rate.

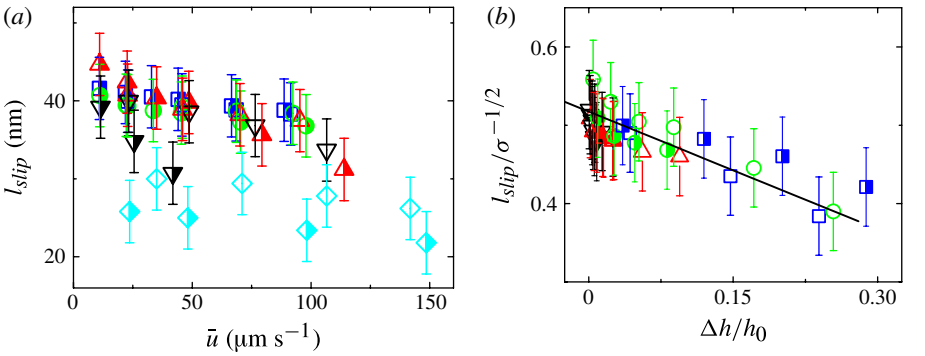

FIGURE 10. (Colour online) Glycocalyx–fluid interface. (*a*) Slip length as a function of the mean velocity across the channel. (*b*) Normalized slip length as a function of the relative decrease of glycocalyx layer height. The solid line represents mean-field calculation results while the open and half-open symbols represent DPD simulation results of 5 and 3 μm channels. The square, circle, upper-triangle, lower-triangle and diamond symbols represent EGL fibre with $EI = 1000, 490, 250, 100, 0$ pN nm^2, respectively.

3.2.4. *DPD simulations of red blood cell suspensions*

Next, we perform simulations of blood flow in a tube of diameter $D = 10$ μm. Blood is modelled as monodisperse, neutrally buoyant, red blood cells (RBCs) in a Newtonian fluid (plasma); white cells and platelets are omitted since they do not change the blood's viscosity in homogeneous shear flow (see Fedosov *et al.* 2011*b*). In particular, we consider blood with 30 % haematocrit, and we model RBCs using a multiscale model, which is also based on the DPD approach (see Fedosov, Caswell & Karniadakis 2010). For a molecular description (spectrin-level) of an RBC model we typically require ∼30000 tight junctions to cover the RBC membrane. However, accurate results have been obtained using even 500 DPD particles to represent the tight junctions (see Fedosov *et al.* 2011*a*). Here we employ very high-resolution models in order to capture the subtle interaction of RBCs with the glycocalyx filaments but also for computational efficiency we used a slightly coarse-grained model with 9128 tight junctions. We consider two blood flow simulations, one without glycocalyx, and one with glycocalyx with height $h_0 = 0.5$ μm and grafting density $\sigma = 108.5$ μm^{-2}. We maintain the same pressure drop for both simulations.

In steady blood flow in a tube, the cross-stream migration of RBCs leads to a central core consisting mainly of RBCs separated from the wall by a cell-free layer (CFL), as shown in figure 11. In this case, RBCs do not interact with the glycocalyx directly. The velocity profiles in the tube blood flow, both with and without glycocalyx, are shown in figure 12(*a*,*b*), with the latter showing details around the CFL and EGL. The presence of the CFL, which is greater than the EGL, implies that our scaling laws inferred from homogeneous flow without RBCs are also applicable to the RBC suspensions. Since the local velocity is smaller than ∼50 μm s^{-1}, and given our findings in figure 10(*a*), the slip length is almost constant and of the order of $1/\sigma^{-1/2}$. This has, in fact, been observed in our simulations with RBCs present.

4. Summary

We employed dissipative particle dynamics (DPD) to model two apparently similar systems, namely flow over surfaces coated with polymer brushes and glycocalyx

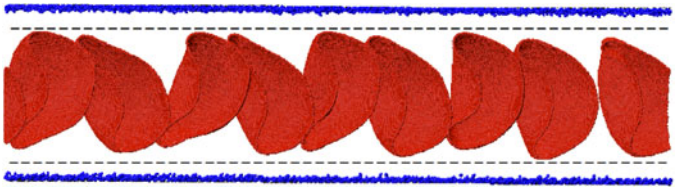

FIGURE 11. (Colour online) DPD simulation of blood flow in a tube ($D = 10\,\mu$m) with deformable red blood cells, shown in grey (red), modelled explicitly. Shown in black (dark blue) are the glycocalyx fibres; while the dashed lines represent the edge of the cell-free layer.

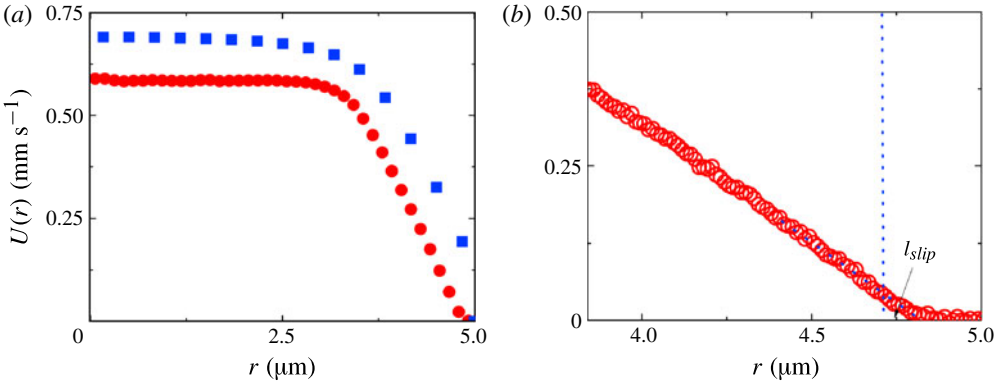

FIGURE 12. (Colour online) (*a*) Velocity profiles in blood flow in a tube with glycocalyx (red circles) and without glycocalyx (blue squares). (*b*) Zoomed view around the cell-free layer.

filaments. We considered both shear-driven and pressure-driven flows, and here, for the first time, we have presented mesoscopic simulations of blood flow bounded by glycocalyx-coated walls interacting with deformable red cells having nearly molecular-scale accuracy. Three-dimensional DPD simulations, although more efficient than molecular dynamics simulations, are time-consuming and hence an exhaustive sensitivity analysis is computationally prohibitive. To this end, we used existing experimental data for validation and mean-field theory for guidance in extracting new scaling laws for the two systems. In particular, we investigated the additional resistance to the flow due to the presence of the flexible or semi-flexible polymer chains, the compression of the height of the polymer brush and glycocalyx fibres, and the slip properties at the free ends of these layers.

There are some common features of the two flow systems but also some surprising differences. Both the polymer brush and glycocalyx layer decrease the effective width of the channel, hence leading to increased pressure drop for given flow rate. However, our simulation results show that the glycocalyx fibres, modelled as semi-flexible polymers with finite flexural rigidity, present higher resistance to the flow than polymer brushes, modelled as flexible polymers with zero flexural rigidity – see figure 8(*a*). The conformational entropy dominates the dynamic properties of polymer brushes, causing a cyclic and tumbling motion of single polymer chains in densely grafted polymer brushes under strong shear flow, with corresponding reversal of the near-surface flow – see figure 6(*b*). On the other hand, the glycocalyx dynamics

is determined primarily by its bending energy, with the glycocalyx fibres vibrating around their equilibrium positions with small amplitude. The height of polymer brushes decreases only slightly (∼5 %) even at relatively large shear rates, whereas the height of glycocalyx decreases substantially (∼50 %) and can be described by a simple scaling law at small Reynolds numbers – see (3.18). The slip length of both polymer brushes and glycocalyx fibres at small shear rate is constant and of the order of $O(\sigma^{-1/2})$ (with σ the grafting density) due to the screening effect of hydrodynamic interactions. However, above a critical shear rate identified in our simulations, the slip length of polymer brushes increases whereas that of the glycocalyx decreases. In both cases we have developed simple scaling laws to represent this dependence – see (3.5) and (3.19).

Finally, we presented here simulations of blood flow in a small tube coated with a glycocalyx layer and interacting with red blood cells (RBCs), which we also model via DPD. We found that, owing to the presence of a cell-free layer (CFL), created by the migration of RBCs towards the tube centre, there is no direct RBC–glycocalyx interaction. Instead, the glycocalyx layer is fully immersed in the CFL, which consists of plasma only, and hence the scaling laws that we derived for homogeneous flow can be used to characterize this case as well. We note, however, that for many haematological disorders the glycocalyx layer may be partially damaged, and hence contact of RBCs with the glycocalyx layer is to be expected in those cases.

Acknowledgements

This work was supported by NSF CBET-0852948 and NIH Grant R01HL094270. H.L. would also like to acknowledge support by the Program of the National Natural Science Foundation of China (NNSFC) Grant 20874094. Simulations were performed at the NSF Supercomputing Center NICS and at BG/P at ANL through an INCITE DOE award.

REFERENCES

ADIGA, S. P. & BRENNER, D. W. 2005 Flow control through polymer-grafted smart nanofluidic channels: molecular dynamics simulations. *Nano Lett.* **5**, 2509.

ALEXANDER, S. 1977 Adsorption of chain molecules with a polar head: a scaling description. *J. Phys. (Paris)* **38**, 983.

ANASTASSOPOULOS, D. L., SPILIOPOULOS, N., VRADIS, A. A., TOPRAKCIOGLU, C., BAKER, S. M. & MENELLE, A. 2006 Shear-induced desorption in polymer brushes. *Macromolecules* **39**, 8901.

AUBOUY, M., HARDEN, J. L. & CATES, M. E. 1996 Shear-induced deformation and desorption of grafted polymer layers. *J. Phys.* II **6**, 969.

BAKER, S. M., SMITH, G. S., ANASTASSOPOULOS, D. L., TOPRAKCIOGLU, C., VRADIS, A. A. & BUCKNALL, D. G. 2000 Structure of polymer brushes under shear flow in a good solvent. *Macromolecules* **33**, 1120.

BARRAT, J. L. 1992 A possible mechanism for swelling of polymer brushes under shear. *Macromolecules* **25**, 832.

BIRSHTEIN, T. M., BORISOV, O. V., ZHULINA, E. B., KHOKHLOV, A. R. & YURASOVA, T. A. 1987 Conformations of comb-like macromolecules. *Polym. Sci. USSR* **29**, 1293.

BRINKMAN, H. C. 1947 A calculation of the viscous force exerted by a flowing fluid on a dense swarm of particles. *Appl. Sci. Res.* **A1**, 27.

BROEKHUIZEN, L. N., MOOIJ, H. L., KASTELEIN, J. J., STROES, E. S., VINK, H. & NIEUWDORP, M. 2009 Endothelial glycocalyx as potential diagnostic and therapeutic target in cardiovascular disease. *Curr. Opin. Lipidol.* **20**, 57–62.

DAMIANO, E. R. 1998 The effect of the endothelial-cell glycocalyx on the motion of red blood cells through capillaries. *Microvasc. Res.* **55**, 77–91.

DAMIANO, E. R., DULING, B. R., LEY, K. & SKALAK, T. C. 1996 Axisymmetric pressure-driven flow of rigid pellets through a cylindrical tube lined with a deformable porous wall layer. *J. Fluid Mech.* **314**, 163–189.

DAMIANO, E. R. & STACE, T. M. 2002 A mechano-electrochemical model of radial deformation of the capillary glycocalyx. *Biophys. J.* **82**, 1153–1175.

DENG, M., JIANG, Y., LIANG, H. J. & CHEN, Z. Y. J. 2010 Wormlike polymer brush: a self-consistent field treatment. *Macromolecules* **43**, 3455.

DOYLE, P. S., SHAQFEH, E. S. G. & GAST, A. P. 1997 Rheology of 'wet' polymer brushes via Brownian dynamics simulation: steady vs oscillatory shear. *Phys. Rev. Lett.* **78**, 1182.

ESPANOL, P. & WARREN, P. B. 1995 Statistical mechanics of dissipative particle dynamics. *Europhys. Lett.* **30**, 191.

FEDOSOV, D. A., CASWELL, B. & KARNIADAKIS, G. E. 2010 A multiscale red blood cell model with accurate mechanics, rheology, and dynamics. *Biophys. J.* **98** (10), 2215–2225.

FEDOSOV, D. A., CASWELL, B., SURESH, S. & KARNIADAKIS, G. E. 2011*a* Quantifying the biophysical characteristics of *Plasmodium-falciparum*-parasitized red blood cells in microcirculation. *Proc. Natl Acad. Sci. USA* **108**, 35–39.

FEDOSOV, D. A. & KARNIADAKIS, G. E. 2009 Triple-decker: interfacing atomistic–mesoscopic–continuum flow regimes. *J. Comput. Phys.* **228**, 1157.

FEDOSOV, D. A., PAN, W., CASWELL, B., GOMPPER, G. & KARNIADAKIS, G. E. 2011*b* Predicting human blood viscosity in silico. *Proc. Natl Acad. Sci. USA* **108**, 11772–11777.

GAO, L. & LIPOWSKY, H. H. 2009 Measurement of solute transport in the endothelial glycocalyx using indicator dilution techniques. *Ann. Biomed. Engng* **37**, 1781–1795.

DE GENNES, P. G. 1980 Conformations of polymers attached to an interface. *Macromolecules* **13**, 1069.

GREST, G. S. 1996 Interfacial sliding of polymer brushes: a molecular dynamics simulation. *Phys. Rev. Lett.* **76**, 4979.

GREST, G. S. 1999 Normal and shear forces between polymer brushes. *Adv. Polym. Sci.* **138**, 149.

GROOT, R. D. & WARREN, P. B. 1997 Dissipative particle dynamics: bridging the gap between atomistic and mesoscopic simulation. *J. Chem. Phys.* **107**, 4423.

GUO, P., WEINSTEIN, A. M. & WEINBAUM, S. 2000 A hydrodynamic mechanosensory hypothesis for brush border microvilli. *Am. J. Physiol. Renal Physiol.* **279**, F698–F712.

HAN, Y., WEINBAUM, S., SPAAN, J. A. E. & VINK, H. 2006 Large-deformation analysis of the elastic recoil of fibre layers in a Brinkman medium with application to the endothelial glycocalyx. *J. Fluid Mech.* **554**, 217–235.

HARDEN, J. L. & CATES, M. E. 1996 Deformation of grafted polymer layers in strong shear flows. *Phys. Rev.* E **53**, 3782.

HOOGERBRUGGE, P. J. & KOELMAN, J. M. V. A. 1992 Simulating microscopic hydrodynamic phenomena with dissipative particle dynamics. *Europhys. Lett.* **19**, 155.

HUANG, J., WANG, Y. & LARADJI, M. 2006 Flow control by smart nanofluidic channels: a dissipative particle dynamics simulation. *Macromolecules* **39**, 5546.

INN, Y. & WANG, S. Q. 1996 Hydrodynamic slip: polymer adsorption and desorption at melt/solid interfaces. *Phys. Rev. Lett.* **76**, 467.

IRFACHSYAD, D., TILDESLEY, D. & MALFREYT, P. 2002 Dissipative particle dynamics simulation of grafted polymer brushes under shear. *Phys. Chem. Chem. Phys.* **4**, 3008.

IVKOV, R., BULTER, P. D., SATIJA, S. K. & FETTERS, L. J. 2001 Effect of solvent flow on a polymer brush: a neutron reflectivity study of the brush height and chain density profile. *Langmuir* **17**, 2999.

KENT, M. S., LEE, L. T., FACTOR, B. J., RONDELEZ, F. & SMITH, G. S. 1995 Tethered chains in good solvent conditions: an experimental study involving Langmuir diblock copolymer monolayers. *J. Chem. Phys.* **103**, 2320.

KIM, Y., LOBASKIN, Y., GUTSCHE, C., KREMER, F., PINCUS, P. & NETZ, R. 2009 Nolinear response of grafted semiflexible polymers in shear flow. *Macromolecules* **42**, 3650–3655.

KLEIN, J., KUMACHEVA, E., MAHALU, D., PERAHIA, D. & FETTERS, L. J. 1994 Reduction of frictional forces between solid surfaces bearing polymer brushes. *Nature* **370**, 634.

KLEIN, J., PERAHIA, D. & WARBURG, S. 1991 Forces between polymer-bearing surfaces undergoing shear. *Nature* **352**, 143.

KREER, T., BINDER, K. & MUSER, M. H. 2003 Friction between polymer brushes in good solvent conditions: steady-state sliding versus transient behaviour. *Langmuir* **19**, 7551.

KUMARAN, V. 1993 Hydrodynamic interactions in flow past grafted polymers. *Macromolecules* **26**, 2464.

LAI, P. Y. & BINDER, K. 1993 Grafted polymer layers under shear: a Monte Carlo simulation. *J. Chem. Phys.* **98**, 2366.

LEI, H., CASWELL, B. & KARNIADAKIS, G. E. 2010 Direct construction of mesoscopic models from microscopic simulations. *Phys. Rev.* E **81**, 026704.

MIAO, L., GUO, H. & ZUCKERMANN, M. J. 1996 Conformation of polymer brushes under shear: chain tilting and stretching. *Macromolecules* **29**, 2289.

MILNER, S. T. 1991*a* Hydrodynamic penetration into parabolic brushes. *Macromolecules* **24**, 3704.

MILNER, S. T. 1991*b* Polymer brushes. *Science* **251**, 905.

MILNER, S. T., WITTEN, T. A. & CATES, M. E. 1988 Theory of the grafted polymer brush. *Macromolecules* **21**, 2610.

MÜLLER, M. & PASTORINO, C. 2008 Cyclic motion and inversion of surface flow direction in a dense polymer brush under shear. *Europhys. Lett.* **81**, 28002.

NARDAI, M. M. & ZIFFERER, G. 2009 Simulation of dilute solutions of linear and star-branched polymers by dissipative particle dynamics. *J. Chem. Phys.* **131**, 124903.

NETZ, R. R. & SCHICK, M. 1998 Polymer brushes: from self-consistent field theory to classical theory. *Macromolecules* **31**, 5105.

PASTORINO, C., BINDER, K., KREER, T. & MÜLLER, M. 2006 Static and dynamic properties of the interface between a polymer brush and a melt of identical chains. *J. Chem. Phys.* **124**, 064902.

PETERS, G. H. & TILDESLEY, D. J. 1995 Computer simulation of the rheology of grafted chains under shear. *Phys. Rev.* E **52**, 1882.

PLIMPTON, S. 2011 LAMMPS: molecular dynamics simulator. http://lammps.sandia.gov.

PRIES, A. R. & SECOMB, T. W. 2005 Microvascular blood viscosity in vivo and the endothelial surface layer. *Am. J. Physiol. Heart Circ. Physiol.* **289**, H2657–H2664.

PRIES, A. R., SECOMB, T. W. & GAEHTGENS, P. 2000 The endothelial surface layer. *Pflugers Arch.* **440**, 653.

PRIES, A. R., SECOMB, T. W., GESSNER, T., SPERANDIO, M. B., GROSS, J. F. & GAEHTGENS, P 1994 Resistance to blood flow in microvessels in vivo. *Circulat. Res.* **75**, 904.

RABIN, Y. & ALEXANDER, S. 1990 Stretching of grafted polymer layers. *Europhys. Lett.* **13**, 49.

SECOMB, T. W., HSU, R. & PRIES, A. R. 1998 A model for red blood cell motion in glycocalyx-lined capillaries. *Am. J. Physiol. Heart Circ. Physiol.* **274**, H1016–H1022.

SECOMB, T. W., HSU, R. & PRIES, A. R. 2001 Motion of red blood cells in a capillary with an endothelial surface layer: effect of flow velocity. *Am. J. Physiol. Heart Circul. Physiol.* **281**, H629–H636.

SEVICK, E. M. & WILLIAMS, D. R. M. 1994 Polymer brushes as pressure-sensitive automated microvalves. *Macromolecules* **27**, 5285.

SQUIRE, J. M., CHEW, M., NNEJI, G., NEAL, C., BARRY, J. & MICHEL, C. 2001 Quasi-periodic substructure in the microvessel endothelial glycocalyx: a possible explanation for molecular filtering? *J. Struct. Biol.* **136**, 239–255.

WEINBAUM, S., TARBELL, J. M. & DAMIANO, E. R. 2007 The structure and function of the endothelial glycocalyx layer. *Annu. Rev. Biomed. Engng* **9**, 121–167.

WEINBAUM, S., ZHANG, X., HAN, Y., VINK, H. & COWIN, S. C. 2003 Mechanotransduction and flow across the endothelial glycocalyx. *Proc. Natl Acad. Sci. USA* **100** (13), 7988–7995.

WIJMANS, C. M. & SMIT, B. 2002 Simulating tethered polymer layers in shear flow with the dissipative particle dynamics technique. *Macromolecules* **35**, 7138.

ZHULINA, E. B., BORISOV, O. V. & PRYAMITSYN, V. A. 1990 Theory of steric stabilization of colloid dispersions by grafted polymers. *J. Colloid Interface Sci.* **137**, 495.

ZHULINA, E. B. & VILGIS, T. A. 1995 *Macromolecules* **28**, 1008.